JOURNAL OF SOLID STATE CHEMISTRY 100, 71–89 (1992)

# Diffuse Scattering in Yttria-Stabilized Cubic Zirconia

T. R. WELBERRY, R. L. WITHERS, J. G. THOMPSON, AND B. D. BUTLER

*Research School of Chemistry, Australian National University, GPO Box 4, Canberra City, ACT 2601, Australia*

Received December 5, 1991; accepted February 28, 1992

We have used a position-sensitive detector (PSD) system to make measurements of the diffuse X-ray scattering on a cubic $Y_2O_3$-stabilized zirconia, $Zr_{0.61}Y_{0.39}O_{1.805}$, in far greater detail than has hitherto been reported. In addition to the fairly prominent diffuse peaks visible in ⟨1 1 0⟩ sections that have been the center of discussion in many previous studies we see a number of other characteristic diffraction features. We report results of some Monte Carlo simulations in which we attempt to find the origins of these various features. We believe one feature, in the form of sets of dark planes normal to ⟨1 1 0⟩, occurs because of *size-effect*-like strains induced along ⟨1 1 0⟩ intermetal vectors, and is only visible because of the similarity of the scattering factors for Zr and Y. A second feature, in the form of *bow-tie*-shaped regions of scattering, originates from the same basic strains but the symmetry of these requires that displacements in the [1 1 0] direction are out of phase with those in the [1 −1 0], implying a distortion of the basic metal coordination such that an expansion along [1 1 0] is accompanied by a contraction along [1 −1 0]. 

## 1. Introduction

The structure of pure zirconia, $ZrO_2$, is reported as being monoclinic from room temperature up to ~1170°C, tetragonal between ~1170 and ~2370°C, and cubic (fluorite type) from ~2370°C up to the melting point at ~2680°C (*13*). The "stabilization" of the high temperature, cubic polymorph of $ZrO_2$ via the addition of a relatively large amount (~5–~50 mole%) of the oxides of a variety of lower valent metals—such as CaO, MgO, $Y_2O_3$, or the lanthanide sesquioxides $Ln_2O_3$–and subsequent quenching from sufficiently elevated temperatures (~1600°C) leads to anion-deficient materials with important ceramic and superionic conduction properties. Such properties are strongly dependent upon the extent of compositional modulation (in the form of the distribution of the metal atoms and the oxygen vacancy ordering) and subsequent associated structural relaxation or displacive modulation. Information as to the type and extent of such compositional and displacive modulation is most directly present in the form of the weak satellite reflections and/or weak diffuse intensity distributions which almost invariably accompany the strong, sharp, Bragg reflections of the underlying fluorite-type average structure (Space group, $Fm3m$, metal atoms on 4(a) (0, 0, 0) and oxygens on 8(f) ($\frac{1}{4}$, $\frac{1}{4}$, $\frac{1}{4}$)).

Numerous workers have attempted to extract reliable information as to the type and extent of such compositional and displacive modulation from a wide variety of electron, X-ray, and neutron diffraction data (*1–12*).



0022-4596/92 $5.00

Several basically different approaches to structural description have been proposed. The first describes (in statistical terms) an atomic environment that is the same at all points, i.e., a split atom model is used and the positions and occupancies of these split atom sites are then refined. Thus, for example, Steele and Fender (*2*) and Morinaga *et al.* (*6*) agree that oxygen atoms in the ~20–30 mole% $YO_{1.5}$ in $ZrO_2$ solid solution are disordered over positions displaced ~0.25 Å from the ideal fluorite oxygen positions along ⟨100⟩ directions. Horiuchi *et al.* (*8*) and Howard *et al.* (*13*), on the other hand, favor ⟨111⟩ rather than ⟨100⟩ oxygen atom splitting. Such a split-atom approach is based on fitting to the average structure diffraction data. Another approach is essentially heterogeneous and treats the structure as an agglomeration of discrete regions of perfect order—such ordered regions being understood to correspond to particular fluorite-related line phases which can sometimes be obtained from a defect fluorite solid solution via prolonged annealing at lower temperatures (*14, 15*). A further approach is based upon a correlated distribution of defect clusters or microdomains within a disordered matrix (*16*). The latter two approaches are based on fitting to the observed diffuse data. Despite extensive investigation by numerous workers over the last 30 years, however, a satisfactory description of such structures has still not emerged.

The lack of consensus among workers regarding the nature of the structure can be attributed in part to the fact that the many investigations have dealt with a whole range of different samples with a diversity of compositions and annealing histories, but it seems likely that many of the difficulties and disagreements stem from the inadequate quality and incomplete nature of the diffuse scattering measurements that have been available. Because of the difficulty of accurate measurement and subsequent interpretation, diffuse intensity distributions have been rather neglected in comparison to investigations based on analysis of Bragg reflections.

We have recently developed (*17*) a position-sensitive detector system for recording diffuse X-ray scattering, which gives an enhancement factor (in terms of data collection times) of ~100 over conventional single counter systems. This system is ideally suited to the measurement of diffuse scattering over large regions of reciprocal space and is particularly suited to nonzero level sections containing no Bragg peaks. In the present work we have used this system to make measurements of the diffuse scattering in a cubic $Y_2O_3$ stabilized zirconia, $Zr_{0.61}Y_{0.39}O_{1.805}$, in far greater detail than has hitherto been reported. Our results clearly indicate that the fairly prominent diffuse peaks visible in ⟨1 1 0⟩ sections and that have been the center of discussion in many previous studies (*9, 16*) are in fact merely cross sections through more extended three-dimensional diffuse features. In addition we observe a number of other definite and distinctive features of the patterns for which any plausible model of the system must be able to account.

In previous papers we have used Monte Carlo simulation techniques together with optical transform methods to aid in the interpretation of the diffuse scattering patterns of a variety of different systems (*18–23*). More recently with the advent of sufficiently powerful modern computers we have begun to replace the optical method, as a means of obtaining the diffraction pattern of a simulated model, by direct calculation (*24*). In the present work we have used these techniques to investigate the possible origin of the features we observe in our $Y_2O_3$-stabilized zirconia sample. While it might initially be supposed that, because yttrium and zirconium have virtually indistinguishable X-ray scattering factors, the system would make a poor choice for an X-ray study, we show that in fact it is just this property of

the system that gives rise to some very characteristic features in the pattern and allows some definite conclusions to be reached.

## 2. Experimental

The sample used for the X-ray study was a sphere of 0.5 mm diameter. This was obtained from a large single crystal sample of composition $Zr_{0.61}Y_{0.39}O_{1.805}$ supplied by the Ceres Corporation. A thin section of thickness ~0.7 mm was first cut from the bulk and then this was further subdivided to yield a number of small cubes of side ~0.7 mm. A Huber crystal grinder was then used to reduce these to a spherical shape. Initial samples using a coarse abrasive had extensive surface damage which gave rise to powder streaking extending a considerable distance from the Bragg peaks, and this precluded the possibility of recording of good quality diffuse scattering data with the PSD system. Several methods were attempted in order to reduce this effect:

(i) grinding the sphere with progressively finer abrasives;

(ii) annealing the ground sphere in air at 1600°C for up to 1 week;

(iii) tumbling the ground sphere in hot concentrated HF for 1–16 hr.

The first of these did not sufficiently reduce the streaking of the Bragg reflections. The second removed the initial streaking completely, but caused the surface to crack, the cracks containing polycrystalline inclusions of another phase which also interfered with measurement of diffuse intensity. The third method also removed the initial streaking of the Bragg reflections, but an opaque, white skin of reaction product, probably on oxyfluoride hydrate, was left on the sphere. However, a few seconds of further grinding of the HF-etched sphere provided a specimen with a tolerable level of powder streaking. Even so, the presence of even this small amount of powder streaking meant that it was not possible to record reciprocal sections containing any Bragg peaks, since the accompanying powder streaking, some of which would be entering the detector at any setting of the crystal rotation $\omega$, tended to swamp the low-level diffuse scattering signal.

The PSD system which utilizes Cu $K\alpha$ radiation and flat-cone Weissenberg geometry allows the collection of data from a whole reciprocal layer normal to the crystal rotation axis with a single setting of the detector. The useful range of diffraction angle covered by the curved detector for a single setting is ~47° of $2\theta$. A larger range may be obtained by combining two sets of data. In the present experiments we used two ranges to give a total coverage from ~23° to 117° (this latter being the maximum possible because of geometrical constaints on the instrument). Because of the relatively high absorption for the 0.5-mm sample at low angles and because the majority of the diffuse scattering in $Y_2O_3$-stabilized zirconia is displacive in origin, it was considered that little useful information would be obtained below 23°.

Although the data obtained from the PSD system is in digital form, the resolution in the reciprocal layer is such that we find it useful for interpretive purposes to display the whole layer in the form of a gray-scale image, first on a computer screen and then subsequently in hard copy form. In this way, features are readily seen which may go unnoticed in for example a contour plot of more coarsely sampled data. In Fig. 1 we show such gray-scale images for sections normal to $\mathbf{c}^*$ in increments of $0.1\mathbf{c}^*$. The resolution along $\mathbf{c}^*$ is limited by the width of the aperture placed in front (and along the length) of the detector. With the slit width of 4 mm that was used in the experiments the resolution is such that the recorded data represents an integration over approximately $\pm 0.05\ \mathbf{c}^*$ of the given section. The resolution within each section is limited by

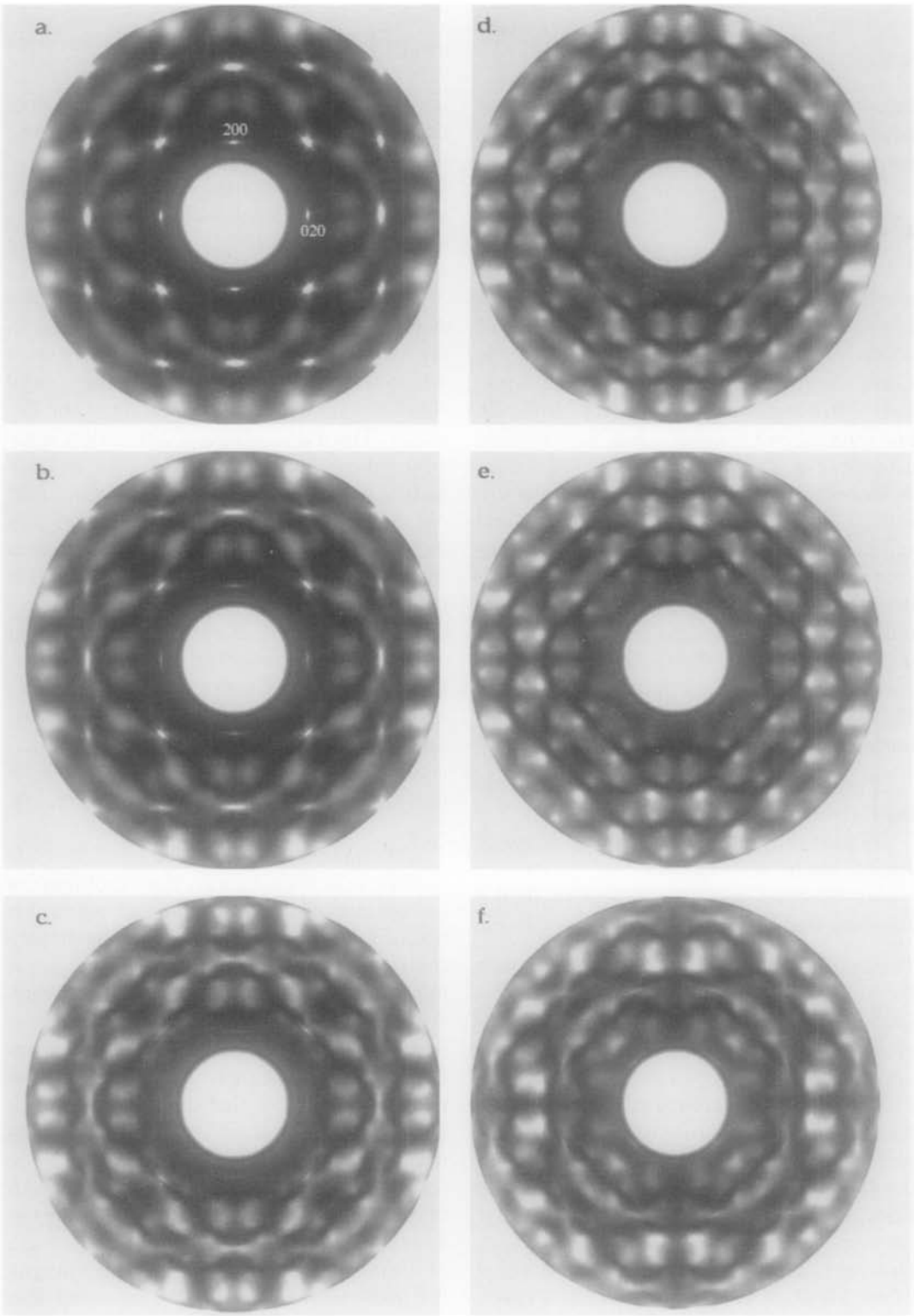


FIG. 1. X-ray diffraction patterns in sections normal to **c*** of yttria-stabilized cubic zirconia, recorded using a position-sensitive detector (PSD) system. The sections are (a) 0.1 **c***, (b) 0.2 **c***, (c) 0.3 **c***, (d) 0.4 **c***, (e) 0.5 **c***, and (f) 0.7 **c***. The outer limit of the recorded data corresponds to ~117° of $2\theta$, using Cu$K\alpha$ radiation. The peaks appearing in the 0.1 **c*** section are caused by powder tails coming from the Bragg peaks in the zero-level section. These serve as a useful reference to mark the scale of all the sections.

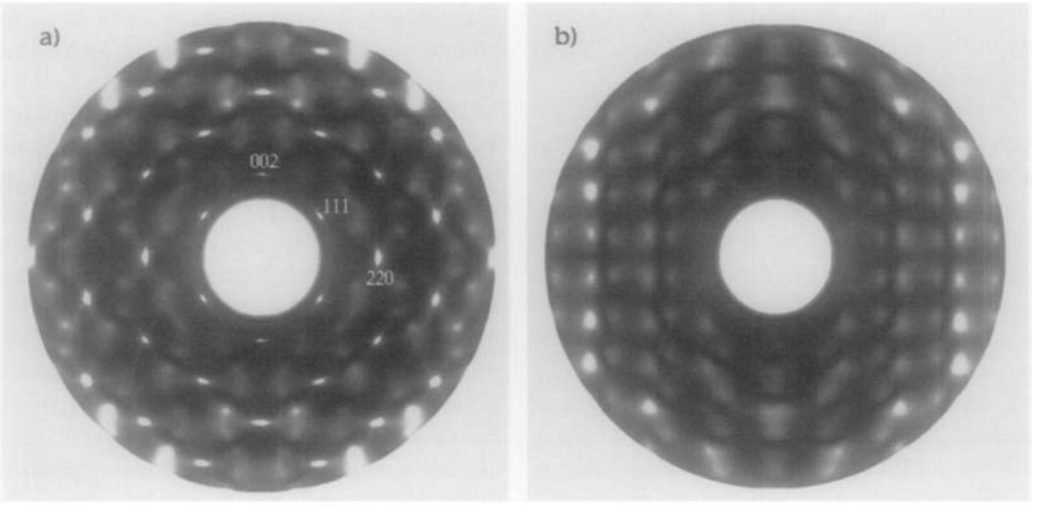


FIG. 2. X-ray diffraction patterns in sections normal to [1 1 0] of yttria-stabilized cubic zirconia, recorded using a position-sensitive detector (PSD) system. The sections are (a) 0.07 (1 1 0)* and (b) 0.5 (1 1 0)*. The outer limit of the recorded data corresponds to ~117° of $2\theta$, using Cu$K\alpha$ radiation.

the sample size and beam divergence and is significantly better (~±0.02 **a*** or **b***). Although these images appear similar to conventional X-ray photographs, their digital origin gives the additional advantage that they are all on the same scale, and each has been treated identically in producing these figures. For further details of the PSD system and the production of such images, see Osborn and Welberry (*17*). In Fig. 2 we show for comparison sections normal to ⟨1 1 0⟩.

## 3. X-ray Patterns

The X-ray patterns shown in Figs. 1 and 2 give a comprehensive view of the diffuse scattering in $Y_2O_3$-stabilized zirconia. The patterns appear very complex with a whole variety of different and distinctive features but which nevertheless are clearly all part of the same single continuous distribution. Most of these features were not observed in previous experimental data, see, for example, Suzuki *et al.* (*9*). It is useful to list these features. In the following summary we refer specifically to the sections normal to **c*** shown in Fig. 1, but the same features can be observed from a different perspective in the sections normal to ⟨1 1 0⟩ shown in Fig. 2.

(i) There are very distinctive dark lines, particularly visible on the 0.4 **c*** and 0.5 **c*** sections, but clearly visible on other sections too. Comparison of different sections shows that these dark lines are in fact planes normal to ⟨1 1 0⟩.

(ii) There are *bow-tie* shaped features which can be seen most clearly in the region of the reciprocal points ($h = 0$, $k = 4$, $l = 0.3, 0.4$), ($h = 4$, $k = 0$, $l = 0.3, 0.4$), and ($h = 5$, $k = 1$, $l = 0.7$). These features clearly extend over a range of **c*** diminishing in intensity toward 0.0 **c***. They have an azimuthal variation which indicates that they arise from correlated longitudinal atomic displacements in the ⟨1 0 0⟩ directions. It was initially thought that these features might originate from cooperative motion of ⟨1 0 0⟩ oxygen "strings," driven by the presence of the ~10% vacancies. While simulations based on such a model could

approximate this feature they failed to generate other characteristic features listed here and were not pursued further.

(iii) Toward 0.5 **c*** the same features are seen to develop pairs of diffuse peaks at the broad extremities of the bow-tie.

(iv) Because of the azimuthal variation, the bow-tie features are not recognizable in the [1 −1 0] and [1 1 0] directions where the two differently polarized effects intermingle. However, here, the diffuse peaks occurring at the extremities of the bow-ties are clearly visible (particularly in the 0.5 **c*** section). These diffuse peaks occur in pairs split by $\sim\pm 0.09\{2, -2, 0\}^*$ on either side of the $\boldsymbol{G}_F \pm \frac{1}{2}\{111\}^*$ positions of reciprocal space in the 0.5 **c*** section. (Here $\boldsymbol{G}_F$ refers to a reciprocal lattice point of the parent fluorite structure). When the azimuthal variation of the intensity of these spots is considered it is clear that they correspond to atomic displacements polarized along [1 −1 0].

(v) Referring to the broad regions of diffuse scattering generally, but also the diffuse peaks in particular, it is noticable that there is a substantial difference in intensity between the low-angle and high-angle sides of the dark lines mentioned in (i), in all cases the region immediately outside the dark line is more intense than that on the inside. Such a transfer of intensity is characteristic of the so-called *atomic size-effect* (*25*).

Our aim in this preliminary study is to try to establish the origins of these different but nonetheless linked diffraction effects.

## 4. Structural Chemical Considerations

The idealized structure of cubic zirconias is based on that of fluorite (Space group *Fm3m*, metal atoms on 4(a) (0, 0, 0) and oxygens on 8(f) $(\frac{1}{4}, \frac{1}{4}, \frac{1}{4})$). Each metal site is at the center of a cube of oxygen sites and cubes along each of the three axial directions are alternatively filled and empty. For the unit cell dimension, **a** = 5.175 Å, of the sample used in our X-ray experiments, the average metal–oxygen distance is $(5.175 \times \sqrt{3} \div 4)$ Å = 2.241 Å. With approximately 10% of oxygen sites vacant we may expect that in a given cube the coordination of the metal will be [8], [7], [6], or even lower, and it is interesting to consider the extent to which the valence of each metal ion is satisfied in these environments. To do this we make use of the bond length–bond valence relationship (see, for example, I. D. Brown (*26*)). This relationship assumes that the contribution, $s$, to the valence of a particular ion by a bond to another ion is given in terms of the bond length, $d$, by the empirical exponential form,

$$s = \exp\left[\frac{(r_0 - d)}{B}\right],$$

where $r_0$ and $B$ are empirically determined parameters, many of which have been tabulated (*27*). $B$ may be taken as a constant for all atom pair types, but $r_0$ has a value characteristic of the particular atom pair. The total valence, $V_i$, of a given atom, $i$, may be obtained by summing over all neighboring atoms, $j$, contributing to the bonding, i.e.,

$$V_i = \sum_j \exp\left[\frac{(r_0 - d_{ij}}{B}\right].$$

Following Brown and Altermatt (*27*), let us assume values of $r_0 = 1.928$ Å for $Zr^{4+}$ with $O^{2-}$ and $r_0 = 2.019$ Å for $Y^{3+}$ with $O^{2-}$, and $B = 0.37$ Å. Then assuming the idealized geometry for the cube, the apparent valences obtained for the two types of metal with [8], [7], or [6] oxygens coordinating, are as given in Table I.

Table I clearly indicates that for a cube of the dimensions of the average experimental value, the Zr atoms are underbonded even when all eight oxygens are present, while the Y atoms are overbonded even if they

TABLE I

THE VALENCE OF Zr AND Y IONS PLACED AT THE CENTER OF A CUBE OF OXYGEN SITES WHEN 8, 7, OR 6 OF THE OXYGEN SITES ARE OCCUPIED

| Atom | Coordination | Valence | Preferred distance (Å) |
|---|---|---|---|
| | [8] | 4.39 | 2.382 |
| Y | [7] | 3.84 | 2.333 |
| | [6] | 3.29 | 2.275 |
| | [8] | 3.43 | 2.184 |
| Zr | [7] | 3.00 | 2.135 |
| | [6] | 2.57 | 2.078 |

*Note.* In the last column is the metal–oxygen distance which would be required for each coordination number for the metal to have the correct valence, c.f. average experimental distance of 2.241 Å.

could all be accommodated in cubes in which there were only six oxygens present.

Thus the simple idealized structure is unstable and must relax in some way to try to accommodate the different valence requirements of the metals. There are two different considerations: first, can the oxygen vacancies be arranged to provide more satisfactory coordination for the two types of metal than would occur for just a random distribution of vacancies; and second, can the individual coordination polyhedra be distorted on a local scale to better satisfy the valences?

For the overbonded yttrium there is no way in which the valence contributions can total 3.0 without an increase in some of the bond distances, even if a coordination of [6] were possible for all the Y atoms. If all bonds were increased equally, for [8] coordination an ~6% expansion would be required, for [7] coordination ~4%, and for [6] coordination ~1.5%. Although it is feasible for the underbonded Zr atoms to obtain additional valence contributions by shifting from the center of the cube (and there is good experimental evidence that Zr is able to tolerate a variety of different bonding geometries and coordination numbers), we find that with the Zr remaining on the cube centre corresponding contractions of 2, 4, and 7% for [8], [7], and [6] coordination, respectively, are required to give the Zr atoms the required valence of 4.0.

It is not uncommon in alloy systems for local "size-effect" distortions of this magnitude to be accommodated by local relaxations (e.g., in $Cu_3Au$ (*25*)), and as a starting point in the present study we investigated the effects of this kind of dilation–contraction distortion on the diffraction pattern of a model system.

## 5. Atomic Size-Effect Distortions

"The atomic size-effect" is the term used to describe the effects of static displacements of atoms in a disordered solid which result from differences in atomic radii. The effect was first described by Warren *et al.* (*25*) and subsequent development of the theory of diffraction from disordered alloys, notably by Borie (*28, 29*), Cowley (*30*), Borie and Sparks (*31*), and Hayakawa *et al.* (*32*), has taken full account of this effect. More recently analagous effects have been investigated by Khanna and Welberry (*33*) for molecular crystals.

Hayakawa *et al.* (*32*) give a general expression for the diffuse scattering from a

disordered alloy which has four different types of term with the forms:

$$I_{\mathrm{SRO}} = \sum_{lmn} \alpha_{lmn} \cos(2\pi l h_1) \cos(2\pi m h_2) \cos(2\pi n h_3) \quad (1a)$$

$$Q_x = -\sum_{lmn} \gamma^x_{lmn} \sin(2\pi l h_1) \cos(2\pi m h_2) \cos(2\pi n h_3) \quad (1b)$$

$$R_x = -\sum_{lmn} \delta^x_{lmn} \cos(2\pi l h_1) \cos(2\pi m h_2) \cos(2\pi n h_3) \quad (1c)$$

$$S_{xy} = -\sum_{lmn} \varepsilon^{xy}_{lmn} \sin(2\pi l h_1) \sin(2\pi m h_2) \cos(2\pi n h_3). \quad (1d)$$

In addition to the $Q_x$, $R_x$, $S_{xy}$ terms listed above there will in general be similar expressions for $Q_y, Q_z, R_y, R_z, S_{yz}, S_{xz}$. In (1a) $\alpha_{lmn}$ are the well-known Warren–Cowley short-range order parameters, which produce cosinusoidal variations of intensity in reciprocal space. These do not depend on the atomic displacements but depend only on the occupancy of the atomic sites. The $\gamma^x_{lmn}$ are the so-called *size-effect parameters* and these produce sinusoidal variations of intensity in reciprocal space and depend on the *average* atomic displacements. The effect of the sinusoidal modulations is to transfer intensity from one side (e.g., the high-angle) of the Bragg peaks to the other (e.g., low-angle). $\delta^x_{lmn}$, $\varepsilon^{xy}_{lmn}$ are higher order terms which depend on the *mean-square* atomic displacements and these give rise to intensity similar to thermal diffuse scattering (TDS). The $\delta^x_{lmn}$ coefficients describe how the $x$-displacement of an atom at the origin is correlated with the $x$-displacement of an atom at the site $lmn$. Similarly the $\varepsilon^{xy}_{lmn}$ coefficients describe how the $x$-displacement of an atom at the origin is correlated with the y-displacement of an atom at the site $lmn$. In addition to having different forms as given by Eqs. (1a)–(1d), these terms have different dependencies on the reciprocal coordinates $\mathbf{k} = (h_1, h_2, h_3)$. Only the short-range-order terms (1a) represent a true Fourier series. For further details the reader is referred to Hayakawa *et al.* (*32*).

For the present case of yttria-stabilized zirconia, a special condition pertains. This arises because the atomic scattering factors for Zr and Y are, for all intents and purposes, indistinguishable. Any terms which depend on the difference of these two scattering factors will be negligible. This is the case for both the $I_{\mathrm{SRO}}$ and $Q_x$, $Q_y$, and $Q_z$ terms in (1)—although this is not immediately apparent in the form of the equations. Consequently, the diffuse intensity that is observed is mostly due to the $R$ and $S$ terms of (1c) and (1d). This is in marked contrast to the usual situation in disordered alloys where the (1a) and (1b) terms are dominant. Indeed, inclusion of the $Q$, $R$, and $S$ terms in analyses has usually been used simply to provide a better fit to observed diffuse scattering so that better estimates for the $\alpha_{lmn}$ may be obtained. Little attention has generally been paid to the $\gamma^x_{lmn}, \delta^x_{lmn}, \varepsilon^{xy}_{lmn}$ parameters themselves.

It should be noted that this (Hayakawa *et al.*'s) description of diffuse scattering distributions is quite general and does not imply any particular mechanism by which the displacements and their correlation fields may have arisen. Our aim in this work is to try to arrive at a physical mechanism which directly leads to a form for the displacement correlation fields which agrees with observation.

Of particular importance in the present study is the recognition that the dark line (plane in 3D) that is seen in the experimental patterns of Fig. 1 and also in the simulation results presented later, is a direct consequence of the coupling of the atomic displacements with the compositional variations, as occurs, for example, in the classical atomic size-effect. This dark-line was observed in a previous optical diffraction study involving the size-effect, (*19*), but no explanation for its origin was given. Hayakawa *et*

*al.* (*32*) had previously noted that the $R$ and $S$ terms gave rise to a "peak depression" beneath the Bragg peaks, but did not seem to recognize the possibility of a "plane of reduced intensity," when the form of the correlation fields is such that the displacements are correlated strongly only along certain specific directions. A detailed description of the origin of this type of dark line is reported elsewhere (*34*).

### 6. 3D Simulation of Simple Size-Effect

To test out the effects of trying to accommodate the different valences of Zr and Y by allowing local expansion and contraction of the coordination cubes we carried out a Monte Carlo simulation on a model system consisting of 32 × 32 × 32 unit cells. To approximate the experimental composition we assumed that there were 10% of the oxygen sites vacant and that 60% of the metal sites contained Zr and 40% Y.

For our initial study, the oxygen vacancies were distributed randomly, but with a constraint that nearest-neighbor (along ⟨1 0 0⟩) and second-nearest-neighbor (along ⟨1 1 0⟩) vacancy pairs were prohibited. This yielded a structure in which ~65% of the metal sites had [7] coordination, ~7% had [6] coordination, and ~27% had [8] coordination. The [8] sites were then filled with Zr, the [6] sites with Y, and the remaining metals were distributed randomly on the [7] sites. With this initial configuration on the undistorted lattice the mean Zr valence was 3.28 ± 0.22 and the mean Y valence was 3.74 ± 0.21. Monte Carlo simulation (see Metropolis *et al.* (*35*)) was then used to relax this structure. This was achieved by applying a harmonic potential for each metal–oxygen bond in each type of coordination with a minimum in the potential at the preferred distance given in Table I; e.g., for Y in [8] coordination the Monte Carlo procedure attempted to make all the Y–O distances equal to 2.382 Å. No other interactions were included in the simulation. After 50 cycles of iteration (a cycle being defined as that number of individual steps required to visit each atom once on average) the structure had relaxed to give the values for bond distances and valences shown in Table II. It is clear from these results that the relaxation has enabled each metal to satisfy its valence requirements reasonably well. The Zr atoms are still somewhat underbonded, but relaxing the constraint that all Zr–O distances within a cube should be the same would allow the Zr to move off-center and achieve a valence close to 4.0. It is worth pointing out that it was found that such relaxation could just as well be achieved if Y was initially put in the [8]-coordinate sites and Zr in the [6]-coordinate sites.

The diffraction patterns of this simulated structure are shown in Fig. 3. The patterns consist of broad planes of diffuse scattering normal to each of the six ⟨1 1 0⟩ directions and clearly visible as bands of intensity on each of the sections normal to [0 0 1]. Within these bands, dark lines similar to those on the experimental patterns can be seen. Also visible in the vicinity of some Bragg peaks there are "bow-tie" shaped features, also reminiscent of those in the experimental patterns. However, these bow-tie features are in the wrong orientation. In the experimental pattern the bow-tie near (4 0 0) is elongated normal to the $x$-axis and that near (0 4 0) normal to the $y$-axis, whereas in the simulated pattern the bow-ties are elongated parallel to the respective axes. A second feature of the patterns which does not correspond to the observed patterns is that the bands are spaced at intervals of 4 × (1 1 0)*, i.e., they pass through (2 2 0)*, (4 4 0)*, etc., whereas in the experimental pattern they occur at intervals of 2 × (1 1 0)*, i.e., passing through (1 1 0)*, (2 2 0)*, (3 3 0)*, (4 4 0)*, etc.

A number of conclusions can be drawn from this preliminary simulation. It is sig-

TABLE II

RESULTS OF THE MONTE CARLO SIMULATION OF A 3D SYSTEM OF 32 × 32 × 32 UNIT CELLS IN WHICH THE ENERGY MINIMUM FOR EACH METAL–OXYGEN BOND WAS AT THE VALUE GIVEN IN TABLE I

| | Before relaxation | After relaxation |
|---|---|---|
| Zr Mean valence | 3.28 ± 0.22 | 3.72 ± 0.34 |
| Y Mean valence | 3.74 ± 0.21 | 2.99 ± 0.05 |
| O Mean valence | 1.92 ± 0.11 | 1.89 ± 0.25 |
| Zr–O [8] distance | 2.24 Å | 2.19 ± 0.28 Å |
| Zr–O [7] distance | 2.24 | 2.15 ± 0.28 |
| Y–O [7] distance | 2.24 | 2.31 ± 0.29 |
| Y–O [6] distance | 2.24 | 2.28 ± 0.08 |

nificant that the main features of the pattern consist of diffuse planes normal to ⟨1 1 0⟩ and with a dark plane running through the middle. The spacing of the planes corresponds in real space to the projection onto [1 1 0] of the Zr–O bond distances along which the size-effect forces were applied. The diffuse bands correspond to the fact that the displacements of individual atoms from their average lattice sites are strongly correlated along rows in the ⟨1 1 0⟩ directions, and the fact that the bands are relatively structureless means that the displacements in neighboring rows are relatively uncorrelated. If a particular bond is longer than the average this produces a strain which is transmitted along the row, but not sideways. The fact that for the set of diffuse bands oriented normal to [1 1 0] the band passing through the origin is absent is indicative of the fact that the correlations are in the same direction as the displacements for this motion. The spacing of the planes in the experimental pattern may correspondingly be attributed directly to forces causing variations in length of the intermetal vectors, Zr–Zr, Zr–Y, or Y–Y, of spacing $\frac{1}{2} d_{110}$.

Because obtaining three-dimensional simulations and their diffraction patterns is computationally very costly, we decide to revert to two-dimensions in order to investigate further the origins of the various observed effects. In the next section we show the results obtained from simulations of a two-dimensional model based on a single layer of the zirconia structure.

## 7. Two-Dimensional Simulations

For the two-dimensional simulations we used a model system as shown in Fig. 4. This may be thought of as representing a single layer of the stabilized zirconia structure. Each small circle represents a superposed pair of oxygen atoms, one above and one below the plane of the metal atoms (depicted by the large circles). A black circle represents a superposed pair of oxygen atoms, one (at least) of which is a vacancy.

As a result of the initial 3D simulation described earlier we concentrate on models in which the dominant effects are caused by interactions between the metal site, i.e., along vectors such as A–B, B–C, C–D, etc.

### *Model 1*

First, we assume that we have a distribution of Y and Zr atoms over the metal sites and then allow the normal size-effect distortions to relax the strain, in an analogous manner to that used in the initial 3D simula-

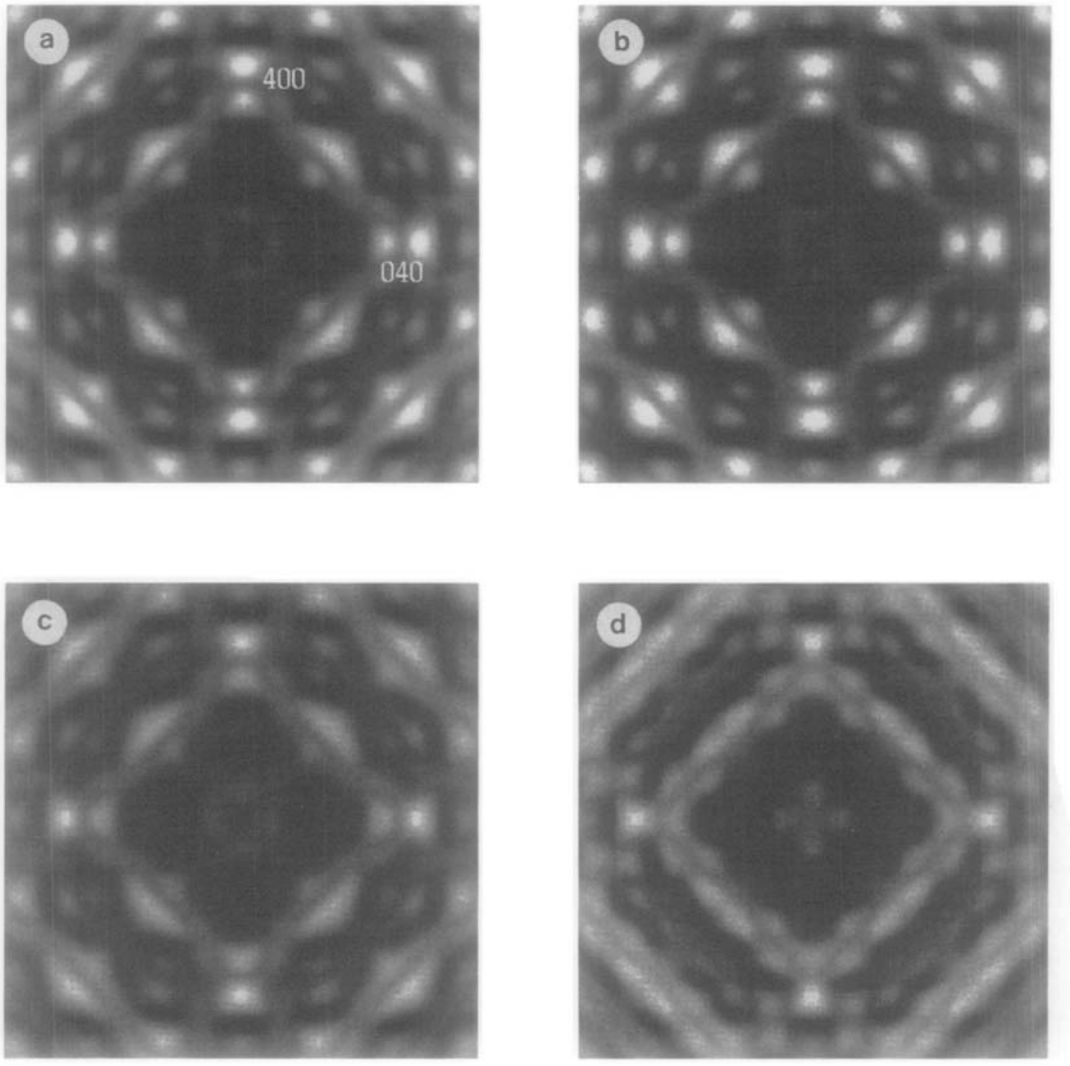


FIG. 3. Sections of a three-dimensional diffraction pattern calculated from the Monte Carlo simulation described in Section 6. Each pattern was obtained by averaging the computed intensity from eight different Monte Carlo runs, each of which contained 32 × 32 × 32 unit cells. (a) Projection onto 0.0 **c*** of whole 3D intensity distribution; (b) 0.1 **c*** section; (c) 0.3 **c*** section; (d) 0.5 **c*** section.

tion. The distribution of the two types of metal was chosen with short-range order included, so that if the scattering factors $f_Y$ and $f_{Zr}$ were appreciably different, diffuse SRO peaks would occur at points approximating those observed in the experimental patterns. This SRO distribution was synthesised using the method described by Welberry and Withers (*36, 37*). In the undistorted lattice such short-range ordering obviously cannot be seen. Size-effect distortions were applied using the Monte Carlo technique with a potential which consisted of a harmonic (Hooke's Law) interaction along the intermetallic vectors A–B, A–D, etc., with a minimum in the separation dis-

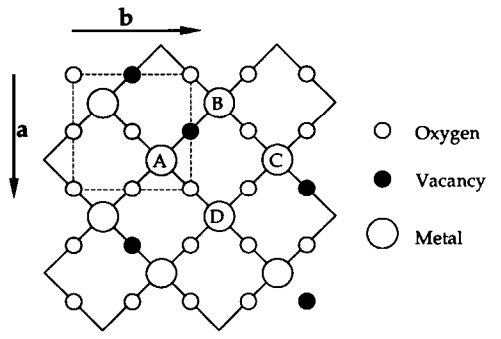


FIG. 4. The 2D model structure used in the simulations.

tance at $(1 + 0.05) \times d_{110}$ for Y–Y; $(1 - 0.05) \times d_{110}$ for Zr–Zr, and $1.0 \times d_{110}$ for Y–Zr. In addition, a weaker restraining force was applied across the diagonals of the basic square of metals (A–B–C–D), since applying forces only along the square edges leads to an unstable framework. This interaction had a force constant of 40% of the main interactions and had its minimum at a separation distance of $d_{100}$ for all atom pairs. A structure giving the diffraction pattern shown in Fig. 5a was obtained. This figure has much in common with the 3D patterns of Fig. 3—diffuse bands normal to ⟨1 1 0⟩ with the same type of azimuthal variation and the dark lines clearly visible within them. Similarly bow-tie like features are to be seen at the points of intersection of the two sets of diffuse planes. This figure demonstrates, however, that application of the distortions to the system containing SRO results in diffuse peaks appearing, even when the two metals have indistinguishable scattering factors. Note also that in the [1 1 0] direction the displacements result in a selection of only four of the peaks that surround a general Bragg position, while in the [1 −1 0] direction the other four peaks are selected. For comparison with Fig. 4a we show in Fig. 4b the analogous pattern obtained when the distribution of Zr and Y atoms on the metal sites is random.

These patterns demonstrate that the symmetry of the distortions produced by this simple size-effect mechanism is wrong. The effects in the [1 1 0] or [1 −1 0] directions taken separately have many of the correct attributes, but where these two effects mix (e.g., around (2 0 0), (4 0 0), etc.) is where the bow-ties appear. The reason for this may be seen in terms of the coefficients $\delta^{x}_{lmn}$, $\varepsilon^{xy}_{lmn}$, in Eq. (1). In our case it is clear that the atomic displacements will be principally along the ⟨1 1 0⟩ directions so for simplicity we will consider the $x$ and $y$ in the coefficients $\delta^{x}_{lmn}$ and $\varepsilon^{xy}_{lmn}$ to be along the [1 1 0] and [1 −1 0] directions, respectively. A positive value of $\varepsilon^{xy}$ would result if the metal atoms labeled B and D in Fig. 4 both move away (or toward) the site labeled A (i.e., the motions tend to be in phase). On the other hand, a negative value of $\varepsilon^{xy}$ would result if the metal atom B moves toward the site A when the atom at D moves away from A or vice versa. Since the sine terms in Eq. (1d) transfer intensity from one side of the line of Bragg peaks to the other, the bow-ties may be described in terms of the intensity being transferred simultaneously from the high to the low side (or vice versa) of the diffuse planes running normal to [1 1 0] and [1 −1 0]. To switch the orientation of the bow-tie we require the effects in the [1 1 0] direction to be out of phase with those in the [1 −1 0] direction. For Figs. 5a and 5b the normal size-effect mechanism dictates that around a given atom the neighbors in the [1 1 0] and in the [1 −1 0] directions will both tend to be displaced either away or toward the atom. What is required for the orientation of the bow-ties to be switched is that when a given atom tends to push away the neighbor in the [1 1 0] direction it simultaneously pulls toward it the neighbor in the [1 −1 0] direction and vice versa.

To demonstrate that this is in fact the case we show in Figs. 5c and 5d patterns obtained using the same distributions of metals that were used for Figs. 5a and 5b. Now, instead

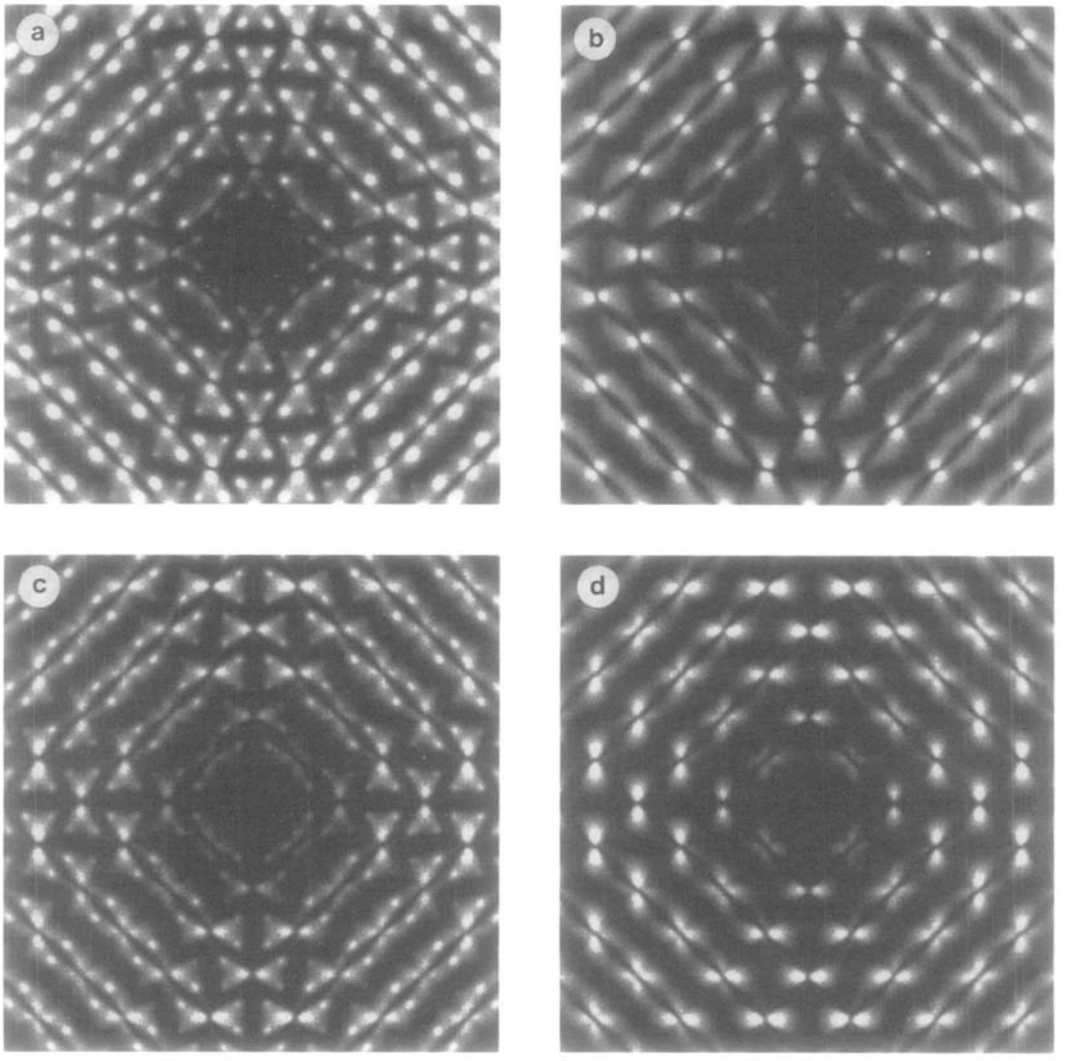


FIG. 5. Diffraction patterns of 2D models in which lattice distortions are applied in two different ways. In (a) and (b) the two types of metal site are treated as though they had atoms of two different sizes which locally expand or contract the lattice. In (c) and (d) the two types of site are treated differently. Sites of one type tend locally to expand the lattice along [1 1 0] and contract it along [1 −1 0]. For sites of the second type the directions of expansion and contraction are reversed. In (a) and (c) the two types of site are distributed with short-range order, but in (b) and (d) the distribution is random. For all the patterns the value of the atomic scattering factor for the different sites is the same, and the intensity arises solely from the atomic displacements. Patterns were calculated from realisations obtained from Monte Carlo simulations of a system of 256 × 256 unit cells.

of the two types of metal being considered to be Zr and Y, respectively, we merely call them all metal, $M$, but distinguish the two types of site as $M1$: those which have a larger than average dimension in the [1 1 0] direction and smaller than average dimension in the [1 −1 0] direction; and $M2$: those which have a smaller than average dimen-

sion in the [1 1 0] direction and larger than average dimension in the [1 −1 0] direction. It is clear that the pattern of Fig. 5c has many of the features that are observed in the various sections of the X-ray data of Fig. 1. The feature that is not produced by this simulation, however, is the transfer of intensity from the low to the high side of the dark lines.

*Model 2*

Although the above model reproduces most of the observed diffraction effects it is unsatisfactory because it is not based on any reasonable physical mechanism. We require, therefore, to find a physically more realistic model which nevertheless encompasses the desirable features of this model.

Instead of allowing the vectors A–B, A–D, etc., to assume different lengths according to whether the two metals involved are Y–Y, Y–Zr, or Zr–Zr, we suppose instead that the length is different according to whether there is an oxygen vacancy (black circle) between the two sites. Thus in Fig. 4, we assume that A–B would be longer than average while A–D, B–C, D–C, etc., would be shorter than average. This may be justified as a mechanism on the grounds that removal of one of the two oxygens would reduce the shielding between the positive charges on the two metals which would therefore tend to move apart. We then see that if we impose the condition that nearest-neighbor (along [1 0 0] or [0 1 0]) vacancies are not allowed, then this mechanism guarantees that the condition that the displacements in the [1 1 0] and [1 −1 0] directions around an atom such as A are out of phase, A–B being longer while A–D is shorter. In order to test this as a viable model we performed a number of simulations in which we ordered the oxygen vacancies in different ways prior to performing the size-effect relaxations. To approximate the experimental condition of ~10% oxygen vacancies in the 3D structure the number of black circles representing a vacancy in a given pair of oxygen sites in the 2D representation was taken as 20%. The ordering was carried out by assigning energies to each of the configurations on the elementary square, a high energy being used to exclude unwanted configurations. This energy could be applied on all squares containing a metal site, all empty squares, or both empty and filled squares. The three examples shown in Fig. 6 are ones in which configurations involving nearest-neighbor, [1 0 0], vacancy pairs were entirely excluded. In Table III we list the frequencies with which each configuration occurred in the Monte Carlo Simulation. Examples (a) and (b) used the same values for the ordering energies. For these two examples the configuration ○● ○○ was given an energy value of zero with all other configurations having a value of 1.0. But whereas in (a) the energy was applied only on the occupied squares, in (b) it was applied on both occupied and unoccupied squares. For example (c) the configuration ○● ●○ was also given an energy of 0.0 and the energies only applied on the occupied squares. It should be noted that these energy values are in arbitrary units since relaxations were carried out at zero temperature.

FIG. 6. Diffraction patterns of three examples of the 2D model of a single layer of the stabilized zirconia structure involving different vacancy ordering schemes. The patterns were calculated from lattice realisations consisting of 256 × 256 unit cells upon which size-effect distortions had been applied (see text for details). (a), (b), and (c) correspond to the examples given in Table III. (d), (e), and (f) show drawings of small portions of the corresponding undistorted distributions. Open circles represent a pair of superimposed oxygen atoms, dark circles represent a pair, one of which is a vacancy, and a cross represents the metal site.

a)

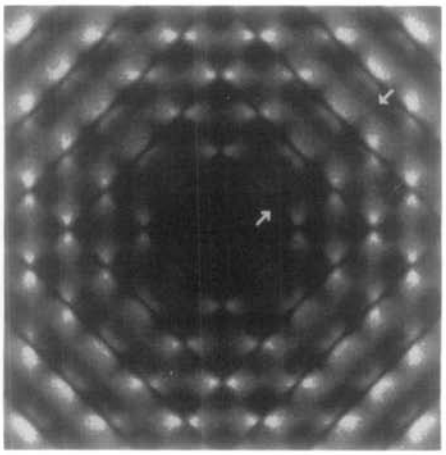

b)

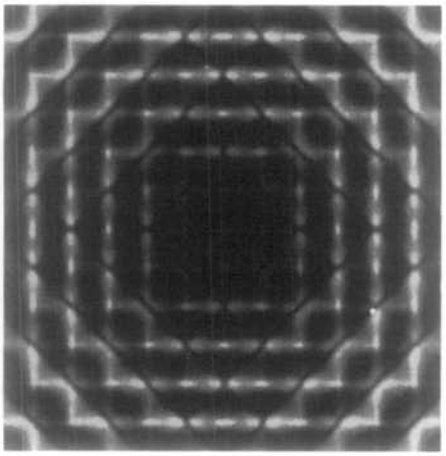

c)

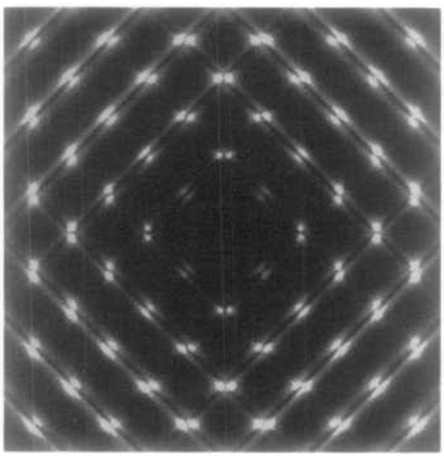

d)

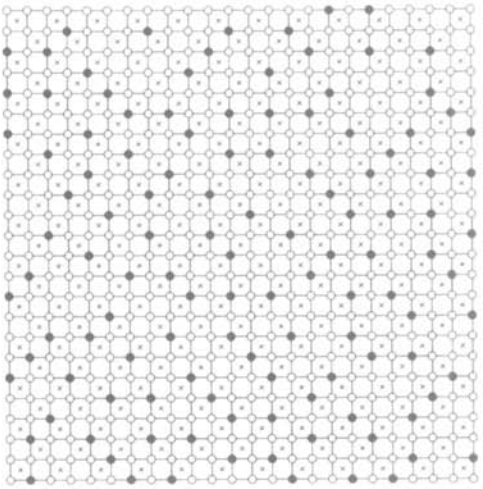

e)

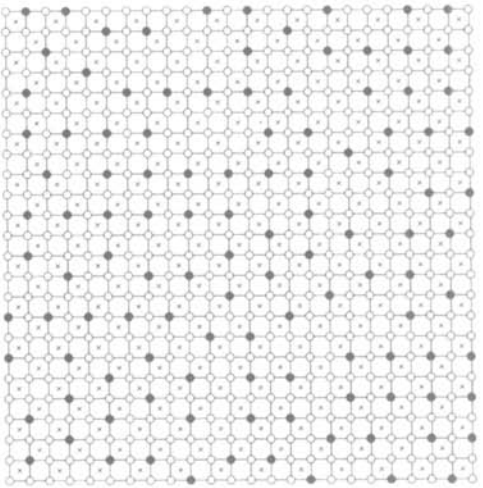

f)

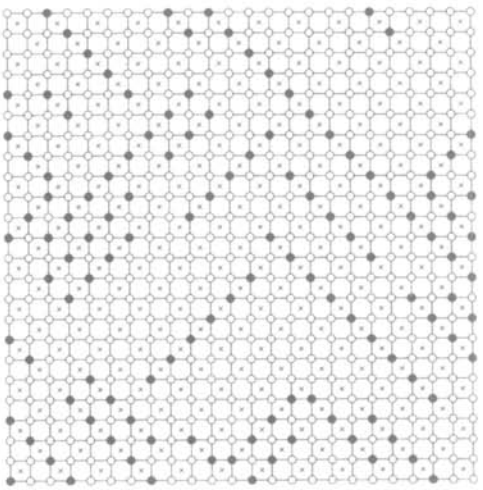

TABLE III

FREQUENCIES WITH WHICH THE DIFFERENT CONFIGURATIONS ON THE ELEMENTARY SQUARE OCCURRED IN THE EXAMPLES SHOWN IN FIG. 6

| | Squares containing metals | | | | Empty squares | | | |
|---|---|---|---|---|---|---|---|---|
| Example | ○○ ○○ | ○● ○○ | ○● ●○ | Other | ○○ ○○ | ○● ○○ | ○● ●○ | Other |
| (a) G1_B | 0.20 | 0.80 | 0.00 | 0.00 | 0.33 | 0.54 | 0.13 | 0.00 |
| (b) G1_E | 0.20 | 0.80 | 0.00 | 0.00 | 0.20 | 0.80 | 0.00 | 0.00 |
| (c) G1_C | 0.52 | 0.17 | 0.31 | 0.01 | 0.32 | 0.57 | 0.11 | 0.01 |

*Note.* Other = ●● ○○ + ●● ●○ + ●● ●●

It is clear from the portions of the realizations shown in Fig. 6 that examples (b) and (c) contain considerably longer-range order than (a). (c) is seen to contain chains of vacancies along the [1 1 0] or [1 −1 0] directions, and (b) contains regions in which a superlattice may be seen with vacancies at the corners of a cell doubled in both the **a** and **b** directions. These examples have been selected from a large number of simulations that were carried out as they illustrate a number of general points that can be made, which we summarize here.

(i) All the simulations show the dark bands normal to [1 1 0] or [1 −1 0] which originate from the basic size-effect forces, despite the quite different diffuse patterns that are obtained with different vacancy ordering schemes.

(ii) All simulations in which nearest-neighbor, [1 0 0], vacancy pairs are avoided show bow-ties in the correct orientation, although the size and detailed shape of these features depends on the particular ordering scheme.

(iii) The more ordered structures, such as 6b and 6c give diffraction patterns containing features which are more highly structured and less diffuse than the more disordered ones, such as 6a.

(iv) It is noticeable in 6a that in the regions of the pattern close to the [1 1 0] and [1 −1 0] directions the diffuse bands are stronger on the high-angle side of the dark line than on the low side, in a similar way to that observed in the experimental patterns (e.g., Fig. 1e). This asymmetry appears to originate from the fact that there are four times as many intermetal vectors that are shorter than average than there are greater than average.

Although example 6a has many features in common with the experimental patterns, the distinctive diffuse peaks are missing. In fact the peaks in the experimental patterns are seen to occur along rows where in this example there is a darker line in the intensity indicated by the arrows in Fig. 6a. Here, the fact that the intensity is stronger along the (1 1 0)* axis and weaker where indicated by the arrows, implies a positive correlation between the [1 1 0]-displacements in neighboring [1 1 0]-rows. In the experimental pattern the presence of the peaks indicates a corresponding negative correlation.

In carrying out these simulations one possibility that has been borne in mind as a possible candidate for a structure on which to base a disordered phase, is the intermediate pyrochlore-type $A_2B_2O_7$. This occurs as a stable phase in a number of fluorite-related systems when the number of vacancies is ~12.5% (although *not*, it should be pointed out, in the $ZrO_2$–$YO_{1.5}$ system itself). In the pyrochlore structure a single layer, as represented by the 2D model described here,

would have alternate [1 1 0] rows containing chains of vacancies and rows containing no vacancies. The vacancies within the chains occur alternately above and below the plane of the metal atoms, but in projection corresponding to the representation of Fig. 4 would have rows containing all black circles. The next layer has these chains running in the [1 −1 0] direction. This pyrochlore-like structure would satisfy the requirement of having displacements in neighbouring [1 1 0] rows negatively correlated, but if the chains are of any substantial length, as they are in the example of Fig. 6c, the diffuse scattering becomes unsatisfactorily narrow.

## 8. Conclusion

In this paper we have reported detailed measurements of the diffuse X-ray scattering distributions in a cubic yttria-stabilized zirconia. In addition we have reported the results of some investigations using Monte Carlo simulation techniques to try to establish the origins of the various diffraction features that are observed in the experimental patterns. At this stage, a full three-dimensional model which entirely accounts for the observed patterns and is consistent with bond-valence requirements for the local microstructure, has not yet been obtained. Three-dimensional simulation and subsequent calculation of sections of a 3D diffraction pattern is computationally expensive and to date we have concentrated on a 2D representation of the structure to obtain insight into the origins of the various diffraction features. However, several important facts have emerged from these investigations and account must be taken of these if a fully satisfactory 3D model is to be found.

The most significant feature of the experimental patterns that is observed is a set of dark planes normal to each of the six ⟨1 1 0⟩ directions and of a spacing equal to the reciprocal of the metal–metal interatomic vector. This feature is observable in yttria-doped zirconia as a result of the fact that the scattering factors for Y and Zr are very similar, and would probably be unobserved in systems displaying first-order scattering effects which depend on the difference in the two scattering factors. We consider that this feature unequivocally demonstrates that lattice distortions due to variations of this fundamental metal–metal distance are the basis for understanding the whole diffraction pattern. The presence of such dark lines in this second-order scattering term (i.e., due to mean-square atomic displacements), is characteristic of atomic size-effect distortions. In the classical "size-effect," local lattice relaxation results in neighboring atoms moving in toward the smaller atoms of a binary mixture or away from the larger atoms, the strain field being propagated outward relatively large distances along rows of atoms. In the present case, however, a second feature of the pattern, in the form of characteristic "bow-tie" shaped regions of scattering, displays a polarization and azimuthal variation that can only be explained if the distortions in two orthogonal directions (e.g. [1 1 0] and [1 −1 0]) are out of phase. That is to say, if an atom tends to push away a neighbor in the [1 1 0] direction, then the corresponding neighbor in the [1 −1 0] direction is drawn inward, and vice versa. We have demonstrated with a simple 2D model system that, with this thesis, each of the different diffraction effects noted in the observed patterns can be obtained.

Despite these encouraging preliminary results some words of caution are appropriate. Although it is clear that the observed effects unequivocally originate from an interaction along vectors corresponding in length and direction to the nearest-neighbor metal–metal spacing, and the symmetry of the motion is such that dilation and contraction in the [1 1 0] and [1 −1 0] are out of phase, it is not inconceivable that an alternative explanation of this motion might be found. Indeed, we are aware that the face-diagonal of the basic cube of oxygen atoms

has exactly the same length and direction as the metal–metal vector, which at this stage seems to be the most important. That nonbonded atomic interactions are important in fluorite-type structures is exemplified by $ZrO_2$ itself which on cooling from >2400°C undergoes successive displacive phase transitions in order to increase its oxygen–oxygen distances. We are also aware that the consensus of opinion, derived from average (Bragg reflection data) structure determination of cubic stabilized zirconias, is that the oxygen atoms are displaced further from the ideal fluorite structure positions than are the metals. It is difficult to know how much credence to attach to these results since there is very little consensus even as to the direction of the displacements. Simple calculation shows that a 5% variation in the metal–metal spacing will produce, at a scattering vector of $\sim 4\mathbf{a}^*$, a scattered intensity from the metals alone which is $\sim 500\times$ the Laue monotonic scattering for the oxygen/vacancy disorder. To produce scattering of a comparable magnitude the oxygen displacements would need to be so large that they would contribute very little at all to the Bragg scattering.

Work is in progress to attempt to incorporate into a 3D model the ideas that have emerged from the current 2D study. The basic problem in proceeding to 3D, apart from the added complexity and greater computation required, is that the effects we have demonstrated originate from the motion along only two of the six ⟨1 1 0⟩ directions. The six ⟨1 1 0⟩ directions are not all mutually orthogonal. Any solution must be an eigenvector of a full 3D force system and cannot be simply derived by superposing three 2D descriptions.

## Acknowledgments

We thank the Australian National University Supercomputer Facility for a generous grant of computer time. We also thank Joseph F. Wenckus, Chairman of Ceres Corporation, for the generous supply of single-crystal samples used in this study.

## References

1. R. E. Carter and W. L. Roth, *in* "EMF Measurement in High Temperature Systems" (C. B. Alcock, Ed.), pp. 125–144, The Institute of Mining and Metallurgy, New York (1968).
2. D. Steel and B. E. F. Fender, *J. Phys. C* **7,** 1 (1974).
3. J. G. Allpress and H. J. Rossell, *J. Solid State Chem.* **15,** 68 (1975).
4. B. Hudson and P. T. Moseley, *J. Solid State Chem.* **19,** 383 (1976).
5. J. Faber, M. H. Mueller, and B. R. Cooper, *Phys. Rev. B* **17,** 4884 (1978).
6. M. Morinaga, J. B. Cohen and J. Faber, Jr. *Acta Crystallogr. Sect. A* **35,** 789 (1979).
7. M. Morinaga, J. B. Cohen, and J. Faber, Jr. *Acta Crystallogr., Sect. A* **36,** 520 (1980).
8. H. Horiuchi, A. J. Schultz, C. W. Leung, and J. M. Williams, *Acta Crystallogr., Sect. B* **40,** 367 (1984).
9. S. Suzuki, M. Tanaka, and M. Ishigame, *Jpn. J. Appl. Phys.* **24,** 401 (1985).
10. N. H. Andersen, K. Clausen, M. A. Hackett, W. Hayes, M. T. Hutchings, J. E. Macdonald, and Osborn, R. *in* "Proceedings 6th Risø International Symposium on Metallurgy and Materials Science" (F. W. Poulsen, N. H. Anderson, K. Clausen, S. Skaarup, and O. T. Sorensen, Eds.), pp. 279–284, The Institution of Mining and Metallurgy, London (1995).
11. N. H. Andersen, K. Clausen, M. A. Hackett, W. Hayes, M. T. Hutchings, J. E. Macdonald, and R. Osborn, *Physica (Utrecht)* **136B,** 315
12. R. B. Neder, F. Frey, and H. Schultz, *Acta Crystallogr., Sect. A* **46,** 799 (1990).
13. C. J. Howard, R. J. Hill, and B. E. Reichert, *Acta Crystallogr., Sect. B* **44,** 116 (1988).
14. J. G. Allpress, H. J. Rossell, and H. G. Scott, *J. Solid State Chem.* **14,** 264 (1975).
15. H. J. Rossell and H. G. Scott, *J. Phys* **38** (12), C7 (1977).
16. R. B. Neder, F. Frey, and H. Schultz, *Acta Crystallogr. Sect. A* **46,** 792 (1990).
17. J. C. Osborn and T. R. Welberry, *J. Appl. Crystallogr.* **23,** 476 (1990).
18. T. R. Welberry, *Acta Crystallogr. Sect. B* **38,** 1921 (1982).
19. T. R. Welberry, *J. Appl. Crystallogr.* **19,** 382 (1986).
20. T. R. Welberry and T. N. Zemb, *J. Colloid Interface Sci.* **123,** 413 (1987).
21. G-L. Hua, T. R. Welberry, and R. L. Withers, *J. Phys. C* **21,** 3863 (1988).

22. T. R. WELBERRY, G.-L. HUA, AND R. L. WITHERS, *J. Appl. Crystallogr.* **22,** 87 (1989).
23. T. R. WELBERRY AND R. L. WITHERS, *Phys. Chem. Miner.* **17,** 117 (1990).
24. B. D. BUTLER AND T. R. WELBERRY, *J. Appl. Crystallogr.* (in press).
25. B. E. WARREN, B. L. AVERBACH, AND B. W. ROBERTS, *J. Appl. Phys.* **22,** 1493 (1951).
26. I. D. BROWN (1981). "Structure and Bonding in Crystals," Vol. II, pp. 1–30, Academic Press, New York (1981).
27. I. D. BROWN AND D. ALTERMATT, *Acta Crystallogr., Sect. B* **41,** 244 (1985).
28. B. BORIE, *Acta Crystallogr.* **10,** 89 (1957).
29. B. BORIE, *Acta Crystallogr.* **12,** 280 (1959).
30. J. M. COWLEY, *Acta Crystallogr., Sect. A* **24,** 557 (1968).
31. B. BORIE AND C. J. SPARKS, *Acta Crystallogr., Sect. A* **27,** 198 (1971).
32. M. HAYAKAWA, P. BARDHAN, AND J. B. COHEN, *J. Appl. Crystallogr.* **8,** 87 (1975).
33. R. KHANNA AND T. R. WELBERRY, *Acta Crystallogr., Sect. A* **43,** 718 (1987).
34. B. D. BUTLER, R. L. WITHERS AND T. R. WELBERRY, *Acta Crystallogr. A* (in press).
35. N. METROPOLIS, A. W. ROSENBLUTH, M. N. ROSENBLUTH, A. H. TELLER, AND E. TELLER, *J. Chem. Phys.* **21,** 1087 (1953).
36. T. R. WELBERRY AND R. L. WITHERS, *J. Appl. Crystallogr.* **20,** 280 (1987).
37. T. R. WELBERRY AND R. L. WITHERS, *J. Appl. Crystallogr.* **23,** 303 (1990).